Available online at www.sciencedirect.com
ScienceDirect
Journal of Computational Physics 224 (2007) 449–463
JOURNAL OF COMPUTATIONAL PHYSICS
www.elsevier.com/locate/jcp

Simulation and measurement of flow generated noise

Peter Moore *, Harmen Slot, Bendiks Jan Boersma

Laboratory for Aero and Hydrodynamics, Delft University of Technology, Leeghwaterstraat 21, 2628 CA Delft, The Netherlands

Received 18 September 2006; received in revised form 30 March 2007; accepted 2 April 2007
Available online 20 April 2007

Abstract

In this paper, we overview our work in developing a numerical approach that allows the complete determination of the dynamic variables and far field sound of subsonic jet flow and a method of experimental validation. We describe the process of direct numerical simulation (DNS) used to determine the jet flow properties in the turbulent region, and combine with the Ffowcs Williams and Hawkings method to obtain far field sound at desired locations. Further, the described method is applied to simulate a Reynolds number 2500, Mach number 0.83 jet, while matching conditions are created experimentally inside a low pressure tank. The mean flow results of the DNS are seen to correspond well with our experimental results, and to be compatible with those published in the literature. The far sound field method is shown to match perfectly with the near sound field obtained by DNS, and sound pressure levels and directivity matches those obtained by us experimentally, and compatible with experimental results previously published.

Keywords: Compressible flow; Navier–Stokes equations; Numerical methods; Jet flow; Computation; Subsonic; Low Reynolds number; Direct numerical Simulation; FFowcs Williams Hawkings method

1. Introduction

Computing power has progressed in recent times allowing in the field of turbulent flow simulation both more complex problems to be studied and simpler problems to be studied more accurately. As the availability of computational power increases, new numerical methods have become necessary to exploit this power to solve the Navier–Stokes equations more accurately. Continuing this trend, the development of new 'direct numerical simulation' (or DNS) methods make possible the complete simulation of a given turbulent flow with moderate Reynolds number by fully solving the Navier–Stokes equations with relevant boundary conditions. Such numerical solutions are complete because they satisfy the Navier–Stokes equations at all flow scales.

Under certain conditions turbulent fluid motions can produce sound. The generation and propagation of sound is governed by the Navier–Stokes equations and a complete compressible DNS calculation in principle determines also the sound component of the total flow motion. A theory describing this phenomena has been

* Corresponding author.
E-mail address: p.moore@wbmt.tudelft.nl (P. Moore, H. Slot, B.J. Boerasma).

0021-9991/$ - see front matter
doi:10.1016/j.jcp.2007.04.006

developed in the middle of the previous century by Lighthill [12]. Lighthill's theory explains how a localized turbulent phenomena in free space can generate an acoustic wave. Simply put, Lighthill rearranged the Navier–Stokes equations of fluid flow to the following form:

$$\frac{\partial^2 \rho}{\partial t^2} - c_\infty^2 \frac{\partial^2 \rho}{\partial x_i \partial x_i} = \frac{\partial^2 T_{ij}}{\partial x_j \partial x_i}, \tag{1}$$

where ρ' is the acoustic density perturbation, c_∞ the ambient speed of sound and T_{ij} the so-called Lighthill stress tensor. This stress tensor is given by

$$T_{ij} = \rho u_i u_j + (p - c_\infty^2 \rho)\delta_{ij} - \tau_{ij}, \tag{2}$$

where τ_{ij} is the viscous stress tensor given by

$$\tau_{ij} = \mu\left(\frac{\partial u_i}{\partial x_j} + \frac{\partial u_j}{\partial x_i} - \frac{2}{3}\delta_{ij}\frac{\partial u_k}{\partial x_k}\right), \tag{3}$$

ρ is the fluid density, u_i the fluid velocity, μ the dynamic viscosity of the fluid, p the acoustic pressure fluctuation and δ_{ij} the Kronecker delta function.

With the rearrangement of terms in the Navier–Stokes equations, Lighthill identifies the possible mechanisms of wave propagation (left-hand side of Eq. (1)) and wave creation (right-hand side of Eq. (1)). Lighthill's equation (1) is integrable using an appropriate Green function, and the result gives the acoustic density ρ' at any location in space and time in terms of flow variables in the turbulent region. Such an approach is very useful because it allows one to determine the acoustic field at locations far away from the source which cannot be determined directly by DNS due to the computational costs associated with accurate solutions in a large domain.

However, the above identification of wave propagation is only truly consistent at low Mach numbers where the flow does not further interact with the acoustic waves after their creation. This identification is thus in effect a simplification that removes such effects as wave convection, diffraction and altered sound speed, which can be common in high Mach number flows and heated flows.

Following Lighthill's approach, several authors have attempted alternative rearrangements of the Navier–Stokes equations, for instance [8,12], in which the interaction between the flow and the acoustic waves are taken into account. However, in general, the complexity of these other acoustic analogons makes them difficult to solve numerically.

An attractive alternative is to use a surface method. Essentially the full, compressible, Navier–Stokes flow is solved on a sufficiently resolved mesh to determine not just the turbulent flow, but also the acoustic waves in some region. The acoustic waves outside this region are then more cheaply determined using either a wave equation designed to use boundary data as acoustic sources (such as Kirchoff surface method or Ffowcs Williams and Hawkings method), or using simplified, cheaper versions of the Navier–Stokes equations optimized to carry acoustic waves (such as the linearized Euler equations). If inside the source region the acoustic waves are accurately determined and all the flow-acoustic interactions are included, then the acoustic waves can be determined accurately in the far field also. Such methods when combined with a complete direct numerical simulation of the flow region in general provide the most accurate predictions (because flow-acoustic interaction effects are automatically dealt with by the flow solver), although are less illuminating with regards to the sound generation mechanisms.

In the study of jet noise phenomenon, direct numerical simulation is only available at low Reynolds numbers, while most realistic flows (such as the jet engine of an airplane) have a much higher Reynolds number. However for both high and low Reynolds number jets, a large amount of the total noise is generated at low frequencies which are related to the specific flow geometry, and the mechanisms by which this occurs are similar in both types of jets. Further, the low frequency noise in jets is generally accepted to be generated by unsteady flow fluctuations, which are generally the most difficult portion of a flow to model accurately. DNS at low Reynolds number is therefore essential to understand noise generation mechanisms and to validate concepts of noise generation that are designed to be used for higher Reynolds number flows.

While the computing power and algorithms required to complete a direct numerical simulation have only been readily available in the last several years, the required computing power required to simulate even a low Reynolds number jet is still fairly restrictive and only a few publications exist using this method (such as [11]). The reason for this difficulty is linked to the nature of acoustic waves in turbulent flows. In general, for a subsonic turbulent flow, the energy associated with acoustic waves is several orders of magnitude lower than the total flow energy. In the past a number of investigators (such as Crighton [5]) have suggested that the acoustic component of the numerical solution of the Navier–Stokes equations would be hopelessly corrupted by numerical errors or even by computational noise itself. For this reason, extremely accurate numerical methods are necessary to compute subsonic flow noise directly, with huge associated computing costs. Still, even today the issue of avoiding numerical errors and computational 'spurious' noise are the main difficulties in obtaining such solutions.

While some experimental data are available at low Reynolds numbers (such as Stromberg et al. [15]), most published experimental data are at high Reynolds numbers. Therefore, simultaneously with DNS of jet capabilities we have been constructing an experimental setup to produce a low Reynolds number, high (but subsonic) Mach number jet flow inside the lab, and take simultaneous measurements of jet flow and acoustic properties. To produce a jet flow under these conditions, the required setup operates at low pressures, and this has been constructed in a manner somewhat similar to that one used in [15].

In this paper we will use a numerical method developed previously [2] to obtain the acoustic far field of a jet and we will compare these results with some experimental findings obtained from our own experimental facility. The organization of the paper is: In Section 2, we will discuss the flow geometry and the numerical solution strategy for the Navier–Stokes equations. In Section 3, we will discuss the continuation of the acoustic field. In Section 4, we will give some results for the flow and the acoustic field. Conclusions follow in Section 5.

2. Geometry, governing equations and numerical procedure

In this section, we discuss the numerical method used to solve the Navier–Stokes equations. This method was developed to be able to solve fully compressible and turbulent flows, so long as no strong shocks are present (such as in the case of supersonic flows). The intended application in this study is to model a high speed (but subsonic) flow with a low (but turbulent) Reynolds number.

To model a jet specifically, appropriate jet boundary conditions are formulated explicitly, while the discretization for the interior of the domain remains applicable to more general flows.

In Fig. 1, we show a sketch of the jet geometry. Air is flowing through a cylindrical nozzle with diameter D and velocity U. Downstream of the nozzle the air flow becomes turbulent and the jet spreading becomes linear. We are particularly interested in flows with Mach numbers approaching 1 which in general are far more noisy than low Mach number flows. At such Mach numbers, compressibility effects become important. The flow is thus governed by the compressible equations for conservation of mass, momentum and energy, see for instance [8]. The equation for conservation of mass reads:

$$\frac{\partial \rho}{\partial t} + \frac{\partial}{\partial x_i} \rho u_i = 0. \tag{4}$$

In which ρ is the fluids density and u_i the velocity vector. The equation for conservation of momentum reads:

$$\frac{\partial \rho u_i}{\partial t} + \frac{\partial}{\partial x_j} [\rho u_i u_j + p\delta_{ij}] = \frac{\partial}{\partial x_j} \tau_{ij}. \tag{5}$$

In which p is the pressure and τ_{ij} is the viscous stress tensor defined in Eq. (3) and the dynamic viscosity μ is in the present study assumed to be constant. The governing equation for the total energy E which is the sum of the internal energy $\rho C_v T$ and the kinetic energy $\rho u_i u_i/2$ reads:

$$\frac{\partial E}{\partial t} + \frac{\partial}{\partial x_j} u_j (p + E) = \frac{\partial}{\partial x_i} \kappa \frac{\partial T}{\partial x_i} + \frac{\partial}{\partial x_j} u_i \tau_{ij}. \tag{6}$$

In which $E = \rho C_v T + \rho u_i u_i/2$ is the total energy, κ the thermal diffusion coefficient. The thermodynamic quantities p, ρ and T are related to each other by the equation of state for an ideal gas

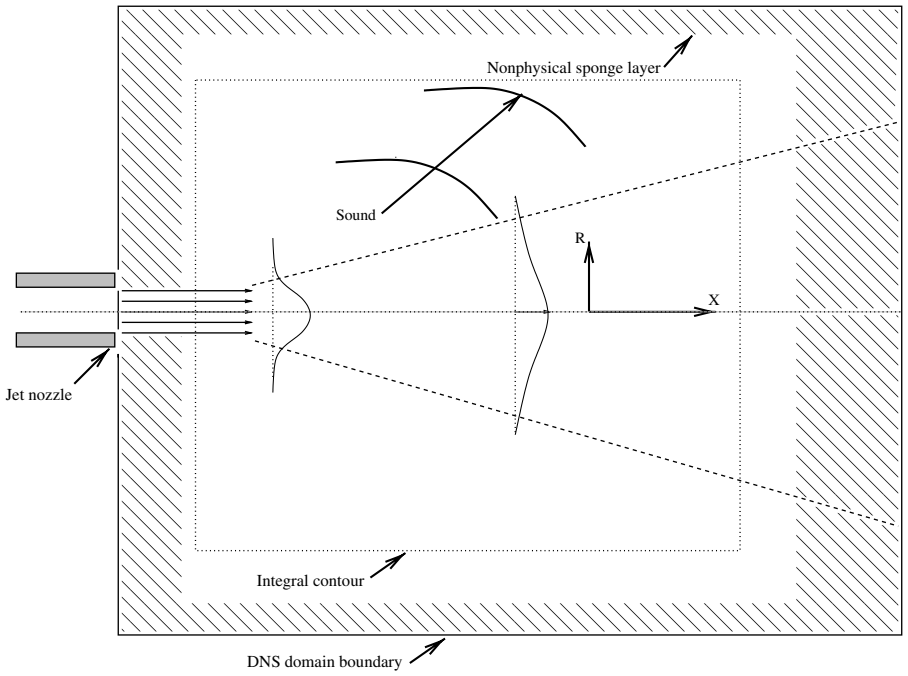

Fig. 1. A sketch of the geometry.

$$p = \rho RT, \tag{7}$$

where R is the gas constant. The speed of sound is defined as:

$$c^2 = \left(\frac{\partial p}{\partial \rho}\right)_s. \tag{8}$$

For an ideal gas it follows that $c = \sqrt{\gamma RT}$ where γ is the specific heat ratio. For an ideal gas the speed of sound is thus only a function of the temperature and of the composition of the gas and independent of the density and pressure!

In solving the equations numerically, all the variables in the equations given above are made non-dimensional using the ambient speed of sound c_∞ as reference velocity scale, the ambient density ρ_∞ as reference density, $\rho_\infty c_\infty^2$ as reference pressure and c_∞^2/C_p as reference temperature. This non-dimensionalization using sound speed is preferred due to the presence of sound waves in compressible flows which must also be captured by the numerical scheme. A second velocity scale is also important in this flow, that of the jet exit velocity U_j. For analysis and description we characterise the flow in this paper using Reynolds number based on jet exit velocity, and with the ambient Mach number, the ratio between the two possible velocity scales:

$$Re = \frac{\rho_\infty U_j D_j}{\mu}, \tag{9}$$

$$Ma = \frac{U_j}{c_\infty}. \tag{10}$$

We will also be reporting on results from other papers which use the exit Mach number of the jet:

$$Ma_{\text{exit}} = \frac{U_j}{c_j}. \tag{11}$$

The numerical method we use is similar to the one used by us before [2]. A staggered formulation has been used. The scalar quantities are stored at the cell centers and the velocity components are stored at the cell faces. All the derivatives are calculated with the following compact finite difference formulation

$$a(f'_{i+1}+f'_{i-1})+f'_i=\frac{b}{\Delta X}(f_{i+1/2}-f_{i-1/2})+\frac{c}{\Delta X}(f_{i+3/2}-f_{i-3/2})+\frac{d}{\Delta X}(f_{i+5/2}-f_{i-5/2})+\frac{e}{\Delta X}(f_{i+7/2}-f_{i-7/2}). \tag{12}$$

In which f'_i is derivative of f with respect to X in point i and ΔX is the grid spacing. The coefficients in the equation above are obtained by Taylor expansions around grid point i. With the five coefficients a, b, c, d and e in Eq. (12) we can obtain an 10th order accurate formulation. The values for a, b, c, d and e for this 10th order scheme are (obtained with the Maple Software package):

$$a=49/190,\quad b=12985/14592,\quad c=78841/364800,\quad d=-343/72960,\quad e=129/851200.$$

For the interpolation between various grid locations we use the following formula:

$$f_i+a(f_{i+1}+f_{i-1})=b(f_{i+1/2}+f_{i-1/2})+c(f_{i_3/2}+f_{i-3/2})+d(f_{i+5/2}+f_{i-5/2})+e(f_{i+7/2}+f_{i-7/2}). \tag{13}$$

In the interior we require again 10th order accuracy resulting in the following values for the coefficients a, b, c, d and e (again obtained with the Maple Software package):

$$a=7/18,\quad b=1225/1536,\quad c=49/512,\quad d=-7/1536,\quad e=1/4608.$$

Both formulations are 10th order accurate in space. Close to the boundaries of the domain the order of the scheme has to be reduced. The exact procedure for this is given in [2].

The time integration of the governing equations has been performed with a standard fourth order Runga–Kutta method, with a fixed time step $\Delta t=c_\infty/100$. The Courant number used in the simulations is approximately 0.7.

2.1. Boundary conditions

The formulation of boundary conditions for aeroacoustic calculations is extremely important. Standard boundary conditions for compressible flow, see for instance Thompson [16] and Poinsot and Lele [14] will always generate some small reflections. These reflections will have no significant influence on the flow field, but will in general have a quite large influence on the acoustic field, which has by definition a very small amplitude. Therefore, we have to use boundary conditions which are 'quiet' i.e. reflection free. In general such a reflection free boundary is constructed by adding layers around the computational domain in which additional terms are added to the equations to damp reflections.

At the in and outflow boundary of the computational domain we add in a small layer an artificial convection velocity U to Eqs. (4)–(6). Here we will show this procedure only for the equation for conservation of mass, Eq. (4)

$$\frac{\partial\rho}{\partial t}+\frac{\partial}{\partial x}(u+U)\rho-\rho\frac{\partial U}{\partial x}=0, \tag{14}$$

where U is the artificial convection velocity. In a very small region close to the in and outflow U is set to a value $U>c$ and smoothly reduced to zero in the interior of the domain. With this modification the flow is thus locally supersonic. This means that at the inflow we can specify velocity, density and total energy as an explicit boundary conditions. At the outflow no conditions have to be imposed, due to the local supersonic nature of the equations. As mentioned before in the interior of the computational domain the artificial convection velocity is zero.

At the lateral boundaries we set all the flow variables to their reference states, this may not be completely correct but the lateral boundaries are positioned far away from the region of interest and an additional damping layer is placed close to the boundaries to damp reflections.

In the damping layers an additional term is added to Eqs. (4)–(6). To be more specific the additional term in the equation for conservation of mass, Eq. (4), is

$$-A(x,y,z)(\rho-\rho_{\text{target}}), \tag{15}$$

where ρ is the regular density as appearing in all the equation $A(x,y,z)$ is a function which is zero in the interior of the computational domain and has small positive values in the damping layer. ρ_{target} is the time averaged (running average) density obtained from the simulations.

3. Acoustic field continuation

The Ffowcs Williams and Hawkings formulation [18] gives the general result for a sound field radiated by turbulence in the presence of arbitrarily moving surfaces. This result is still useful when the surfaces in question are stationary and even when the surfaces are virtual (as opposed to solid), as pointed out in the original paper [18], and later by Francescantonio [7], meaning the result can be applied to problems involving free surface shear. One of the interesting features of this theory is that there are no assumptions made about the nature of the sound source, as opposed to solutions based on Lighthill's acoustic analogy [12], for example, where often to solve the analogy, the speed of sound is assumed constant everywhere and the presence of velocity and temperature gradients are ignored or modeled. In addition, for problems in which the source region is not acoustically compact, storage requirements become formidable in the case of Lighthill's formulation, but remain tractable for the case of Ffowcs Williams Hawkings integration.

It is instructive to outline the derivation of these equations for the specific form we will use here. We begin with Eqs. (4) and (5) which govern the entire flow, both the complicated turbulent region, and the flow surrounding this region. Now suppose we choose a surface S described by $f(\mathbf{x},t)=0$ which encloses some region of the flow (chosen to be the complicated turbulent region). Further we set the flow inside the surface S to the rest state defined by $p'=0$, $\rho=\rho_\infty$ and $\mathbf{u}=0$, so that the flow is now discontinuous across the surface S. The new set of momentum and mass equations that holds in both regions is determined using generalized function theory as

$$\frac{\partial p}{\partial t}+\frac{\partial}{\partial x_i}(\rho u_i)=\rho u_n\delta(f) \tag{16}$$

and

$$\frac{\partial}{\partial t}(\rho u_i)+\frac{\partial}{\partial x_j}((p-p_\infty)\delta_{ij}-\sigma_{ij}+\rho u_i u_j)=[(p\delta_{ij}-\sigma_{ij})n_j+\rho u_i u_n]\delta(f), \tag{17}$$

where u_n is the normal velocity at the surface S. Doing this is essentially maps all the effects of the interior complicated turbulent region to the surface S. These equations can be combined in a standard way to form the following wave equation:

$$\left(\frac{\partial^2}{\partial t^2}-c_\infty^2\frac{\partial^2}{\partial x_i^2}\right)(\rho-\rho_\infty)=\frac{\partial}{\partial t}(\rho u_n\delta(f))-\frac{\partial}{\partial x_i}(L_{ij}n_j\delta(f))+\frac{\partial^2 T_{ij}}{\partial x_i\partial x_j}, \tag{18}$$

where

$$L_i=(p-p_\infty)\delta_{ij}\mathbf{n}_j+\rho u_i u_n, \tag{19}$$

$$T_{ij}=\rho u_i u_j+\left[p-p_\infty-c_\infty^2(\rho-\rho_\infty)\right]\delta_{ij}, \tag{20}$$

$\mathbf{n}_j$ is the unit normal, u_i and u_n are flow velocities, ρ is density, p is pressure, the subscript ∞ represents the ambient value of the given quantity, T_{ij} is Lighthill's stress tensor and the effects of viscosity have been ignored. Eq. (18) can be integrated with a free space Green function. It is only at this final step of integration using a free space Green function that full generality is lost. The requirement of flow linearity at the surface location by the Kirchoff surface method is much weaker in this case, allowing the placement of the surface S in the turbulent and/or shear regions provided the nonlinearities there are not too strong. The final form of this procedure used in the calculation of far field jet sound is

$$p(\mathbf{x}',t')=\frac{1}{4\pi}\frac{\partial}{\partial t}\int_S\left[\frac{\rho u_n}{r}\right]_{t=t'-\frac{r}{c_\infty}}\mathrm{d}A+\frac{1}{4\pi c_\infty}\frac{\partial}{\partial t}\int_S\left[\frac{L_r}{r}\right]_{t=t'-\frac{r}{c_\infty}}\mathrm{d}A+\frac{1}{4\pi}\int_S\left[\frac{L_r}{r^2}\right]_{t=t'-\frac{r}{c_\infty}}\mathrm{d}A, \tag{21}$$

where variables with a $'$ indicate the position and time of the acoustic wave, $r=|\mathbf{x}-\mathbf{x}'|$ is distance from flow point to the acoustic wave, while the volume integration of the stress tensor for sources outside the control surface is neglected. More details of this are found in [7].

Eq. (21) is a series of surface integrals over the surface enclosing the known turbulent sources (illustrated in Fig. 1) and whose solution calculation requires that the fluctuating quantities (velocity, pressure and density)

are known with enough accuracy to describe the acoustic waves present at that boundary. Compressible DNS as described in the previous section can provide these fluctuating quantities, providing a two-step technique for the determination of the far field sound, limited only by the presence of flow outside the computational domain and under resolved structures if insufficient resolution is present.

3.1. Experimental setup

Compressible DNS can only be performed for flows with rather low Reynolds number and high Mach number. To experimentally create a low Reynolds number, high Mach number flow for comparison purposes, we can either make the nozzle size very small, reduce the ambient pressure to create a low density flow, or use a highly viscous fluid. Manipulating the ambient pressure turns out to be the easiest approach to take. This can be done by constructing a chamber in which the ambient pressure is reduced to a fraction of atmospheric pressure, the setup is shown in Fig. 2. The chamber has a cylindrical shape and is 1 m in diameter and is currently 2.8 m in height. The height of the tank can be adjusted through the removal or addition of several segments.

To generate the required conditions, a vacuum pump lowered the pressure inside the chamber to 21 mbar. The flow into the chamber was controlled by a massflow controller at the inlet and a (controllable) vacuum pump at the outlet of the pressure chamber, and proceeded vertically into the chamber through an 8 mm jet nozzle positioned in the chamber floor. Semi-anechoic conditions inside the chamber are created by padding the walls with acoustic dampening material.

Acoustic data are collected from microphones positions on a padded metal arc centered above and pointing towards the jet nozzle. The arc holds 16 microphones at 42 jet diameters from the jet nozzle, equally spaced at angles from 10° to 85° from the jet axis. Data acquisition is performed by two PCI 4472 measurement cards, each capable of simultaneously sampling 8 channels at 100 kHz. A sampling frequency of 65,536 Hz was used.

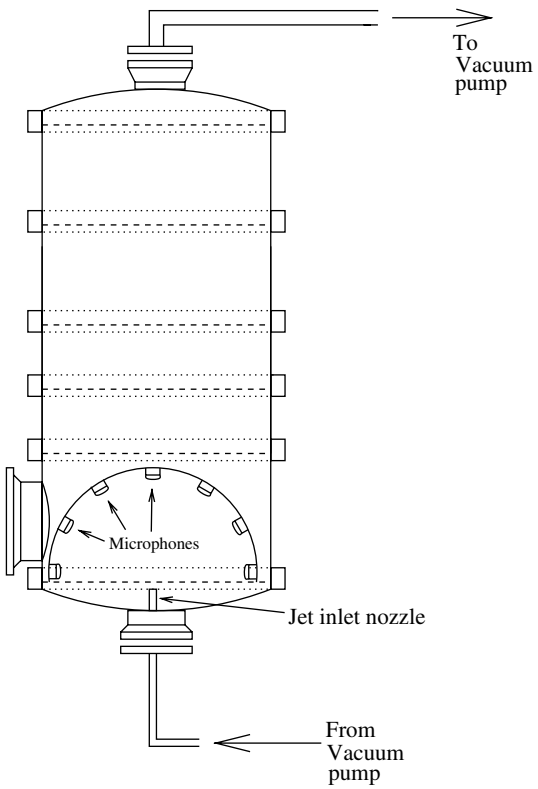

Fig. 2. Schematic of experimental setup.

3.2. Error analysis

In this section a brief error analysis is given for the acoustic measurements. Acoustic measurements were performed using Sonion 8000 series microphones. Their frequency response is nearly flat up to 11 kHz, which makes them suitable for doing aeroacoustic measurements on high speed subsonic jets. The calibration of the microphones is performed by means of a pistonphone. This procedure has to be performed at reduced ambient pressure as the characteristics of the microphones change with decreasing ambient pressure. Below a certain threshold value the acoustic performance of the Sonion microphones is dominated by the acoustic impedance of the microphone membrane, which is independent of ambient pressure. Therefore, below this threshold the microphone's sensitivity is a constant. All microphones were calibrated below this threshold value and all measurements were performed well below this threshold value (threshold value estimated to be around 80 mbar).

Errors in the calibration of the microphones cause an error in the SPL data. The starting point for the analysis is the equation that relates the applied acoustic pressure p_{rms} (Pa) to the rms output of microphones V_{rms} (V) via the microphone sensitivity s (V/Pa) and amplification A,

$$p_{\mathrm{rms}} = \frac{V_{\mathrm{rms}}}{s \cdot A}. \tag{22}$$

The uncertainty in the recorded sound pressure p is scaled up to an uncertainty in the corresponding sound pressure at ambient conditions, which is dependent chiefly upon the accuracy of the chamber pressure measurement through

$$p_{\mathrm{rms}}^{\mathrm{scaled}} = \left(\frac{p0}{p_{\mathrm{chamber}}}\right) \cdot p_{\mathrm{rms}}. \tag{23}$$

The uncertainty in the SPL data due to inaccuracies in microphone sensitivity s and amplification factors A is estimated to be 0.5 dB.

The jet exit velocity is deduced from knowledge of a few variables neatly contained in

$$U_j = \frac{\phi R}{Sp} \cdot \left(T_{\mathrm{s}} - \frac{\gamma - 1}{2} \frac{U_j^2}{\gamma}\right), \tag{24}$$

where U_j is the jet exit velocity, ϕ the jet massflow (kg/s), S the nozzle cross-sectional surface area (m^2), T_{s} the jet stagnation temperature (K) and p is the chamber pressure (Pa). Besides errors in microphone calibration, the uncertainties in quantities such as massflow, temperature and chamber pressure have an effect on the exit Mach number and thus also on the accuracy of the SPL data.

The far field p_{rms} is related to the exit velocity U_j by

$$p_{\mathrm{rms}} \propto \frac{\rho U_j^4 D}{c_\infty^2 R}. \tag{25}$$

From the above analysis we estimate the uncertainty in SPL due to error in jet exit velocity to be 0.44 dB.

Wall reflection effects become increasingly larger with increasing angle to the jet axis. To evaluate the effect of wall reflection effects on acoustic measurements, an ambient jet exiting from a 2.0 mm nozzle with similar far field sound pressure levels was created. Near the wall, there was an observed difference of 2 dB between the free jet and the tank enclosed jet. This error in SPL is estimated from measurements close to the wall and its magnitude diminishes moving towards smaller angles away from the wall. Even though the spectral content of the ambient jet is different to the one created in the experiment, the effect of reflections on acoustic measurements is considered to be representative for the experimental situation.

Overall, an error of 1 dB can be assumed in the SPL data for small angles with an increase to a maximum error of 3 dB for near wall data.

3.3. Numerical setup

A jet of Reynolds number 2500 and Mach number 0.83 (based on jet inflow velocity and c_∞) was simulated using the method described above.

Following [11], the jet inflow velocity profile is specified as

$$U_{\text{in}}(r) = \frac{U_j}{2}\left[1 - \tanh\left(B\left(\frac{r}{r_0} - \frac{r_0}{r}\right)\right)\right], \tag{26}$$

where $B = 12.5$ is a parameter related to the inverse of the initial momentum thickness, r_0 is half the jet diameter width and r is the distance from the jet axis. We found that without added instability to the flow that the turbulent breakup of the jet does not occur until far downstream, increasing significantly the cost of the calculation.

We introduce instabilities to the flow in the same manner as [10,11] where the procedure is given in some detail. The parameter B is also the same chosen by [11]. However due to the lower Reynolds number of this simulation, jet breakup does not occur until a significantly further downstream distance than that in [10,11]. The motivation behind these choices, described in detail by [10,11], is valid for this calculation also.

The computations were performed on a non-uniform Cartesian grid consisting of $330 \times 160 \times 160$ points. In the two directions perpendicular to the jet axis, grid spacing is lowest along the jet axis, and increases toward the domain boundaries. The grid spacing is identical for these two directions. In the axial direction, grid spacing was lowest just after the breakup of the laminar core and highest in the core region, and downstream directions.

In order to determine the axial grid spacing, the calculation was first run several times on grid domains truncated in the directions perpendicular to the jet axis. This allowed us to locate the position of the laminar core breakup, which is not known a priori. It was found from these simulations that the location of laminar core breakup was largely independent of the axial grid spacing given the same turbulent seeding method.

Shown in Fig. 3 is every sixth line of the grid for the axial dimension and one of the perpendicular dimensions. Also shown is the physical portion of the domain. Outside this region, flow is forced to fixed field values. Further, at the boundary downstream of the jet, the flow is filtered in the axial direction.

The number of grid points chosen, combined with the small size of the domain mean and low Reynolds number mean that peak resolution inside the fully turbulent region is approximately 10 times the flow Kolmogorov length scale. Such resolution is consistent with a description of this calculation as a direct numerical simulation. The staggered grid numerical scheme used is naturally diffusive so that no filtering or turbulence modeling is necessary for numerical stability.

The code has been made parallel through the use of the message passing interface (MPI) library. The calculation has been performed partly on an AMD-Opteron system with 8 CPUs and partly on various numbers of processors (up to 104) of the TERAS supercomputer, a 1024-CPU system consisting of two 512-CPU SGI Origin 3800 systems. The simulation required approximately 15 days running time.

For the acoustic post-processing, the 2-D Simpsons rule (third order) is used for the spatial integration while time derivatives are calculated using a five point difference method (third order accuracy). In order to

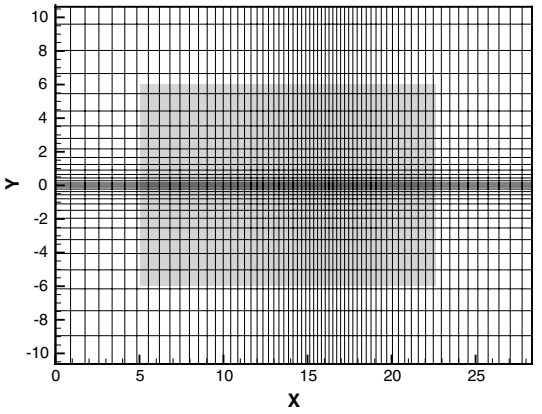

Fig. 3. Two dimensions of the computational grid. Every sixth line is shown in each dimension. Central removed section is the physical portion of the domain.

include retarded time effects accurately in the calculation, the DNS was first completed, and about 30 gigabytes of data was stored for post-operation.

4. Results

4.1. Flow field

In this section, we give results for the jet obtained numerically and experimentally, and compare with the previously published results of [15,11]. Both of these jets had an exit Mach number $Ma_{\text{exit}} = 0.9$ and Reynolds number 3600. The corresponding ambient Mach number for these jets was $Ma = 0.83$. Stromberg's data were obtained experimentally, while Freund's data are the result of direct numerical simulation (see Table 1).

In Figs. 4 and 5, we represent the simulated jet in two and three dimensions through contours of density and vorticity respectively. These figures illustrate the behavior of the turbulent jet: just downstream of the nozzle (upper right in Fig. 4, left center in Fig. 5) the flow is laminar. In the shear layer surrounding the laminar

Table 1
Jet operating conditions of an ambient Mach number 0.83 jet with $Re = 3600$ as presented in this paper

$T_s = 293$ K	Jet stagnation temperature
$\phi = 2.71 \times 10^{-4}$ kg/s	Jet massflow
$M_{\text{exit}} = 0.9$	Exit Mach number
$M_\infty = 0.828$	Ambient Mach number
$Re = 3600$	Reynolds number
$p_c = 18.6$ mbar	Test chamber pressure

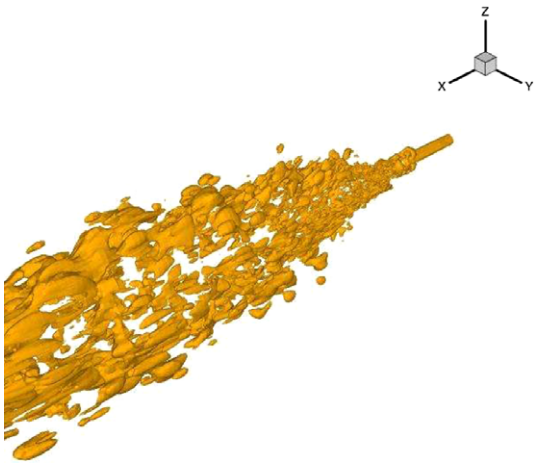

Fig. 4. A 3-D isocontour of the density, $\rho = 1.0005\rho_\infty$.

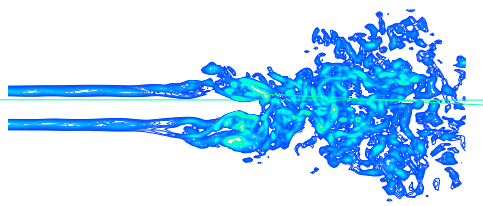

core, instabilities grow until they overwhelm the core region and the flow transitions to turbulent. Downstream the jet spreads at a linear rate as could be expected from standard turbulence theory.

In Fig. 6, we compare the centerline velocity profile determined by our DNS and by us experimentally with a Pitot tube (outer diameter 1.0 mm) with the results of [15,11]. To obtain Fig. 6 each jet was shifted until the end of the respective potential core aligned visually with that of the data from Stromberg [15]. The difference in core breakup position for each case is expected because the flow origins of each DNS are virtual origins not corresponding to the DNS boundary (owing to the presence of buffer layers), and because the initial inducement of the turbulence is dependent on flow seeding and initial momentum shear thickness. However, once correction for the flow origin is made, it is anticipated that the acoustic fields should then be comparable, which originate mainly from the mixing region of the jets, although discrepancies in the acoustic field may also occur if certain types of disturbances in the flow exist [3], or if the momentum shear thickness differs (see Fig. 7).

The agreement shown in Fig. 6 is very good. The main differences between our experimental data and our DNS can be accounted for by the unreliability of the Pitot tube which ignores the possibility of back flow in low speed regions and the radial motion of the jet near the end of the potential core. Importantly in Fig. 6 both our DNS and experimental data match nicely downstream, an indication that the turbulence is accurately being simulated. The decay rates of our jets are determined by fitting the expected downstream decay profile (27) to each with the fit to the DNS also shown in Fig. 6.

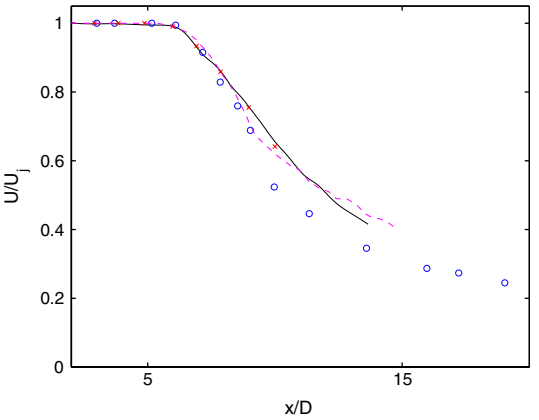

Fig. 6. Centerline velocity profiles. '○' experimental data of Stromberg, '×' our experimental data, '–' our DNS, '–·' fit of Eq. (27), and '– –' is DNS of Freund.

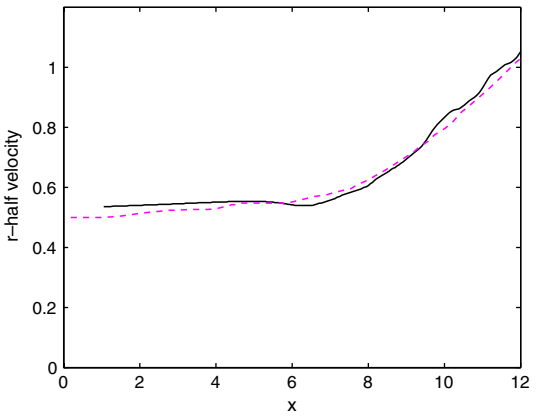

Fig. 7. Half velocity radius. '○' experimental data of Stromberg, '–' our DNS.

$$\frac{U_c}{U_{in}} = \frac{B_u}{x - x_0}. \tag{27}$$

The obtained decay rates B_u were, respectively, 5.37 and 5.22 for the DNS and for the experimental jet. This is consistent with an expectation of between 5.0 and 5.9 (cf. [1]).

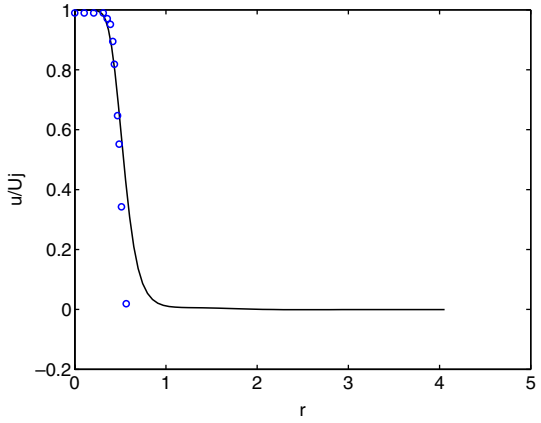

Fig. 8. Radial velocity at $x = 1$.

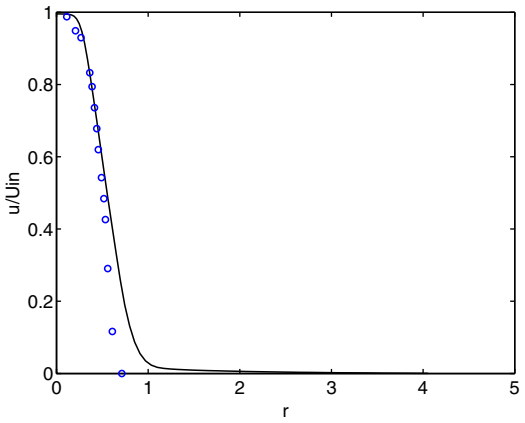

Fig. 9. Radial velocity at $x = 5$.

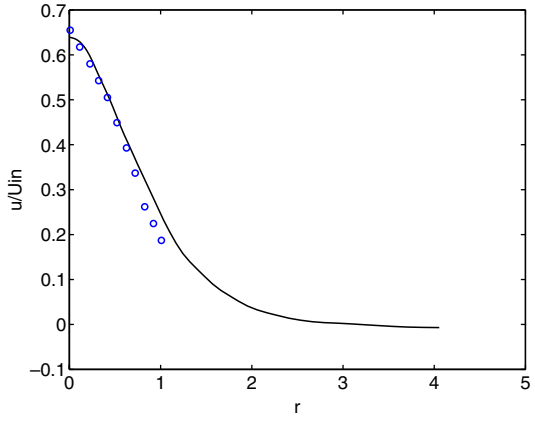

Fig. 10. Radial velocity at $x = 10$.

In Figs. 8–10, we compare radial velocity profiles of our DNS with those of [15]. The profiles obtained are consistent with downstream spreading of the jet. Incidentally, our DNS overshoots the data of [15] when the velocity ratio is below about 0.4. Similar results are reported for the DNS of [11], which are attributed to inaccuracies in Pitot tube measurements at low flow speeds.

4.2. Acoustic field

The most obvious first step to make is to verify that the FWH predictions are consistent with the aeroacoustic field obtainable directly by the use of DNS. It is possible to obtain a complete extended field (from near to far) by using a combination of near field acoustic pressure obtained by the DNS region, and far field acoustic pressure obtained by the FWH formulation. Fig. 11 is a two-dimensional slice of this complete sound region. In this plot, aeroacoustic contours are obtained by the DNS inside the black box, and by FWH outside the black box. These are overlaid by a representation of the jet through its axial velocity.

Next the sound pressure levels and directivity are compared for our DNS and experimental data again with the jets of Freund [11] and Stromberg et al. [15] at a radius of $30.0D_j$ in Fig. 12. The figure shows sound pressure levels represented on a polar plot with the downstream direction at 0° and upstream at 180°. Sound pressure levels of our DNS are averaged azimuthally at each chosen polar angle. Our experimental data were obtained at a radius of $r = 42.0D_j$ and scaled back to $30.0D_j$.

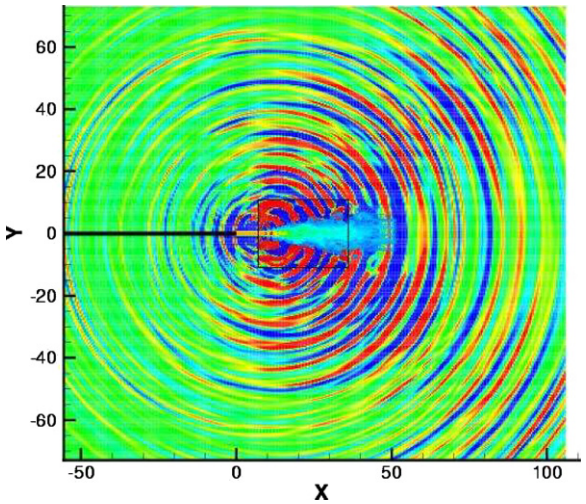

Fig. 11. Instantaneous acoustic pressure contours for jet with velocity in axial direction superposed, showing power of combined method.

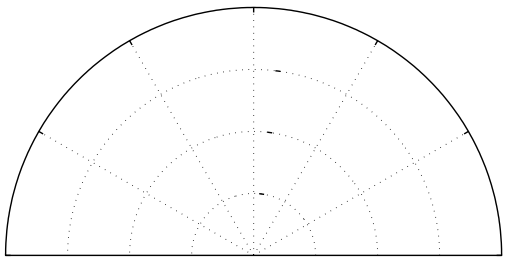

Here the agreement is quite good. The jets of Freund and Stromberg are have ambient Mach number 0.835 ($Ma_{\text{exit}} = 0.9$).

Our experimental results confirm the results obtained by Freund and Stromberg. The experimental data were obtained to match these jets rather than the conditions of the DNS because obtaining data at Reynold's number 2500 and $Ma = 0.83$ required with our given nozzle a pressure lower than we can currently generate. Future results using a smaller nozzle will be able to reproduce our DNS conditions. The results of our DNS confirm that lowering the Reynolds number has little effect on sound pressure levels and directivity.

5. Conclusion

A numerical procedure to obtain the complete flow and sound field of turbulent flows has been outlined and applied to the case of a turbulent jet. The numerical procedure consists firstly of a direct numerical simulation code, which solves the Navier–Stokes equations using a high order compact finite difference formulation on a staggered grid with standard fourth-order Runga–Kutta method for time advancement. When the simulation resolution is high enough, no spatial filtering is necessary due to the numerical stability of the arrangement. In the implementation for jet flow simulation, an artificial convection velocity is added in the boundary regions to ensure local supersonic conditions, while artificial damping terms are added to the equations of motion in the boundary region to suppress unwanted spurious reflections. The physical interior region is unaffected by these modifications. Secondly, in order to compute far-field sound, we have implemented the Ffowcs Williams and Hawkings method which enable sound to be computed independently at arbitrary locations based on knowledge acquired by the DNS of the flow history in the turbulent region. Lastly, we have constructed a large anechoic chamber which can be evacuated to low pressures, allowing the possibility to create low Reynolds number flows through control of the flow density. This setup allows us to make simultaneous flow and sound measurements for jets of low Reynolds number and high Mach number.

Finally, we presented results of a Reynolds number 2500, Mach number 0.83 jet obtained numerically and a Reynolds number 3600, Mach number 0.83 jet obtained experimentally, and compared with previously published experimental and numerical results of Reynolds number 3600, $Ma_{\text{exit}} = 0.9$ jets (where the ambient $Ma = 0.835$). The centerline velocity profiles and sound pressure levels of our simulation compared well with our experimental and the previously published results, and a discussion of this was given.

It is hoped that the combination of a complete jet simulation and simultaneous experimental measurements of the flow and acoustics of the same phenomena will allow us to investigate more deeply the underlying mechanisms by which noise is created in turbulent flows.

Acknowledgment

This project was financially supported by the Dutch Technology Foundation STW under Grant No. DSF:6181.

References

[1] Bodony, D., Lele, S., 2004. Jet noise prediction of cold and hot subsonic jets using large-eddy simulation, AIAA Paper 3022.
[2] B. Boersma, A staggered compact finite difference approach for the compressible Navier–Stokes equations, J. Comput. Phys. 208 (2005) 675–690.
[3] B. Boersma, G. Brethouwer, F. Nieuwstadt, A numerical investigation on the effect of the inflow conditions on the self-similar region of a round jet, Phys. Fluids 10 (1998) 899–909.
[5] D. Crighton, Computational aeroacoustic for low Mach number flows, in: J.C. Hardin, M.Y. Hussani (Eds.), Computational Aeroacoustics, Springer, New York, 1993.
[7] P. Di Francescantonio, A new boundary integral formulation for the prediction of sound radiation, J. Sound Vibr. 202 (4) (1997) 491–509.
[8] M. Goldstein, Aeroacoustics, McGraw-Hill, New York, 1976.
[10] J.B. Freund, Direct numerical simulation of the noise from a Mach 0.9 jet, ASME FEDSM 99-7251, 1999.
[11] J.B. Freund, Noise sources in a low-Reynolds-number turbulent jet at Mach 0.9, J. Fluid Mech. 438 (2001) 277–305.
[12] M. Lighthill, On sound generated aerodynamically, part 1: General theory, Proc. Roy. Soc. Lond. A 211 (1952) 564–587.
[14] T. Poinsot, S. Lele, Boundary conditions for direct simulation of compressible flows, J. Comput. Phys. 101 (1992) 104–129.

[15] J. Stromberg, D. Mclaughlin, T. Troutt, Flow field and acoustic properties of a mach number 0.9 jet at a low reynolds number, J. Sound Vibr. 72 (1980) 159–176.
[16] K. Thompson, Time dependent boundary conditions for hyperbolic systems, J. Comput. Phys. 68 (1987) 1–24.
[18] J. Williams, D. Hawkings, Sound generated by turbulence and surfaces in arbitrary motion, Proc. Roy. Soc. Lond. A 264 (1969) 321–342.

Further reading

[4] B.J. Boersma, S.K. Lele, Large eddy simulation of a mach 0.9 turbulent jet, AIAA Paper 1874, 1999.
[6] N. Curle, The influence of solid boundaries upon aerodynamic sound, Proc. Roy. Soc. Lond. A 231 (1955) 505–514.
[9] M. Howe, Theory of Vortex Sound, University Press, Cambridge, 2003.
[13] P. Moore, B. Boersma, 2005. Use of surface integral methods in the computation of the acoustic far field of a turbulent jet, in: Proceedings of Direct and Large Eddy Simulation, p. 6.
[17] A. Uzun, G. Blaisdell, A. Lyrintzis, Coupling of integral acoustics methods with LES for jet noise prediction, AIAA Paper 0517, 2004.